Cell, Vol. 122, 735–749, September 9, 2005, Copyright ©2005 by Elsevier Inc. DOI 10.1016/j.cell.2005.06.043

Rab Conversion as a Mechanism of Progression from Early to Late Endosomes

Jochen Rink,[1] Eric Ghigo,[1,2] Yannis Kalaidzidis,[1,3] and Marino Zerial[1,*]

[1]Max Planck Institute of Molecular Cell Biology and Genetics
Pfotenhauerstrasse 108
01307 Dresden
Germany

[2]Unité des Rickettsies CNRS UPRES A6020
Faculté de Médecine
27 boulevard Jean Moulin
13385 Marseille Cedex 05
France

[3]A.N. Belozersky Institute of Physico-Chemical Biology
Building A
Moscow State University
Moscow 119899
Russia

Summary

The mechanisms of endosome biogenesis and maintenance are largely unknown. The small GTPases Rab5 and Rab7 are key determinants of early and late endosomes, organizing effector proteins into specific membrane subdomains. Whether such Rab machineries are indefinitely maintained on membranes or can disassemble in the course of cargo transport is an open question. Here, we combined novel image-analysis algorithms with fast live-cell imaging. We found that the level of Rab5 dynamically fluctuates on individual early endosomes, linked by fusion and fission events into a network in time. Within it, degradative cargo concentrates in progressively fewer and larger endosomes that migrate from the cell periphery to the center where Rab5 is rapidly replaced with Rab7. The class C VPS/HOPS complex, an established GEF for Rab7, interacts with Rab5 and is required for Rab5-to-Rab7 conversion. Our results reveal unexpected dynamics of Rab domains and suggest Rab conversion as the mechanism of cargo progression between early and late endosomes.

Introduction

The endocytic system of eukaryotic cells embraces a complex network of membrane compartments, each fulfilling a specific set of tasks in cargo sorting, distribution, and catabolism (for review, see Conner and Schmid, 2003; Gruenberg and Maxfield, 1995; Mellman, 1996; Pelkmans and Helenius, 2003). After internalization in early endosomes, cargo to be recycled (exemplified by the transferrin receptor [TFR] or low-density lipoprotein receptor [LDLR]) returns to the cell surface via recycling endosomes, whereas cargo destined for degradation (epidermal growth factor receptor [EGFR] or low-density lipoprotein [LDL]) is transferred to late endosomes and, ultimately, to lysosomes. However, whereas there is a broad consensus on the organization of the endocytic pathway in terms of organelles and trafficking routes, the mechanisms whereby transport occurs from one endosomal compartment to another are still unsolved, as reflected by the different views formulated over the years. On the one hand, vesicular transport has been the general mechanistic paradigm, proposing that cargo moves by means of vesicles between distinct compartments of stable identity (Geuze et al., 1988; Griffiths and Gruenberg, 1991; Helenius et al., 1983; Palade, 1975; Schekman and Orci, 1996). On the other hand, compartment maturation has been evoked as an alternative transport mode, with the membrane enclosing the cargo progressively changing its composition (Helenius et al., 1983; Murphy, 1991), as observed during phagocytosis (Vieira et al., 2002; Henry et al., 2004). The traditional experimental repertoire, including morphological analysis of fixed specimens, subcellular fractionation, and in vitro transport assays, could not unambiguously distinguish between the aforementioned scenarios. A more suitable approach to address this long-standing problem would be the direct visualization of the dynamics of the endosome trafficking machinery, an approach brought within reach by recent advances in live-cell-imaging techniques.

Besides vesicle coats and adaptors, SNAREs and Rab GTPases have been identified as central regulators of intracellular transport. Both SNAREs and Rab GTPases occur as large families in eukaryotic genomes (Bock et al., 2001), are enriched in specific membrane compartments, and participate in virtually every membrane trafficking reaction (Sollner et al., 1993; Zerial and McBride, 2001). Rab GTPases mediate membrane tethering upstream of SNARE-mediated fusion (Rothman and Sollner, 1997; Zerial and McBride, 2001) and function as membrane organizers by regulating a plethora of soluble effector molecules. Rab5 provides a striking example of the aforementioned principle, recruiting different effector proteins that oligomerize within a membrane domain enriched in PI(3)P (Christoforidis et al., 1999; McBride et al., 1999). Rab5, Rab4, and Rab11 occupy distinct membrane domains sequentially traversed by recycling cargo (Sonnichsen et al., 2000). Late endosomes also consist of separate Rab7 and Rab9 domains (Barbero et al., 2002), and cargo destined for degradation is first internalized into Rab5 domains on early endosomes and later appears in Rab7 domains on late endosomes. Thus, from a molecular viewpoint, transport between endosomes can operationally be defined as transport of cargo between membranes harboring different Rab machineries.

An important consideration in relation to the mechanisms of such transport is that the Rab machinery is peripherally associated with the membrane in a dynamic equilibrium that depends on the balance between guanine nucleotide exchange factors (GEFs) and GTPase-activating proteins (GAPs). In principle, such a

*Correspondence: zerial@mpi-cbg.de

dynamic GDP/GTP cycle could confer two completely different modes of function to the Rab machinery, being indefinitely maintained or remodeled along with the flow of cargo. In light of both the inherent dynamics of Rab domains and their suitability as compartmental identity markers, the question pertaining to the mechanism of transport from early to late endosomes can be rephrased as follows: is the Rab5 domain on early endosomes stably maintained or dynamically assembled and disassembled in the course of cargo transport? Is cargo transferred from stable Rab5-positive early endosomes to Rab7-positive late endosomes, or do Rab5-positive membranes eventually lose Rab5 and acquire Rab7?

Discriminating between these two functional modes depends on the ability to study the dynamics of the Rab machineries on endosomes in the course of cargo transport. However, this is not a trivial task due to the high frequency of short- and long-range movements of endosomes on actin and microtubule filaments (Gasman et al., 2003; Nielsen et al., 1999), which make their tracking increasingly difficult over long periods of time. We overcame this problem here by combining fast live-cell-imaging techniques with the development of new software tools to visualize and quantify the dynamics of membrane bound Rab5 and Rab7 during the transport of LDL from early to late endosomes.

Results

Live-Cell Imaging and Rab-Domain Tracking

To probe the dynamics of Rab5 domains on early endosomes, we used an A431 cell line stably expressing moderate levels of GFP-Rab5 (1- to 5-fold over endogenous; Sonnichsen et al., 2000). Because these cells display neither enlarged endosomes, as under Rab5 hyperactivation (Stenmark et al., 1994), nor alterations in the kinetics of transferrin uptake and recycling (Sonnichsen et al., 2000), GFP-Rab5 can be expected to faithfully reflect the dynamics of the endogenous protein. We developed an experimental strategy (Figure 1A) to track early endosomes over long periods of time by combining high-speed 4D imaging with novel tracking algorithms (see Movie S1 and the Supplemental Experimental Procedures in the Supplemental Data available with this article online; Y.K., unpublished data). The imaging protocol did not cause any appreciable photodamage to the cells. First, cells did not contract but often continued to expand. Second, photobleaching of GFP over 30 min was below 20% of the total signal (Figure S1E). Third, endocytosis was not compromised since cells continued to internalize LDL throughout the experiment (see below). The accuracy of the tracking algorithm was ascertained by systematically comparing computer-generated with manually followed endosome tracks. Based on 200 endosomes from three different sequences, we estimated that the program correctly tracked a structure between successive frames with a probability of 99.4%. Premature track termination accounted for the majority of errors. Wrong connections occurred only in 0.08% of cases (Figures S2A–S2C). Using GFP-tagged rotavirus-like particles as standards (Charpilienne et al., 2001; Figure S2D), we estimated that the smallest visible structures contained ~300 molecules of GFP-Rab5. Reliable tracking required a minimum of 630 (±150, n = 3) molecules. Whereas the majority of endosomes contained 2–3 × 10^3 molecules of GFP-Rab5, the few brightest and biggest structures harbored ≥2 × 10^4 (Figure S2D). Most importantly, immunofluorescence microscopy of the very same structures previously visualized by high-speed imaging (Figure 1C) showed that they corresponded to essentially the entire complement of EEA1-positive membranes, thus establishing that the tracked structures were bona fide Rab5-positive early endosomes.

Stability of Rab5 Domains on Early Endosomes

Depending on whether Rab5 domains are permanent/long-lived or transient assemblies, two main scenarios can be envisaged. Transient assemblies would be indicated by GFP-Rab5 traces undergoing "fade in" and "fade out" (gradual brightening from/dimming to background level). Permanent association, on the other hand, would be incompatible with such events. Figure 1D shows the fluorescence-over-time traces of six exemplary endosomes, all tracked over 7 min and longer. Two conclusions could be drawn from this analysis. First, the half-life of Rab5-positive early endosomes is in the range of 2 min, as deduced from the distribution of track lengths (data not shown). However, since 70% of tracks are terminated by homotypic fusion events (Movie S1), these data indicate that the bulk of early endosomes are not subjected to rapid turnover. Second, the amount of Rab5 associated with a given endosome was unexpectedly found to vary considerably over time, as GFP-Rab5 fluorescence exhibited strong fluctuations (Figures 1D and 2C). We can rule out the possibility that these fluctuations are imaging artifacts: (1) fluctuations are out of phase, excluding changes in laser intensity; (2) they occur over tens of seconds, making movements between focal planes an unlikely cause; and (3) in two color tracks (see below, Figure 3C), they are not paralleled by fluctuations in cargo fluorescence.

We next attempted to identify possible causes of these fluctuations by a close inspection of the image sequences. Interestingly, the frequent sharp upstrokes in a trace could mostly be attributed to a fusion event with another GFP-Rab5 endosome (Movie S2). We estimated that an early endosome undergoes up to two homotypic fusion events per min. However, despite such high frequency, the fluorescence signal of individual endosomes did not increase in a stepwise manner, as fusion events were generally followed by rapid (~40–80 s) loss of GFP-Rab5 from the membrane. This was not mediated by visible fission events, which were observed, albeit with much lower frequency than fusions. Therefore, either fission of vesicles escaping detection or extraction of Rab5 from the membrane via Rab-GDI could explain such removal. We favor the latter since the loss of Rab5 often proceeds without a detectable change in diameter of the structure (see below), inconsistent with scission.

Importantly, loss of Rab5 can proceed to apparent completion, as illustrated by the progressive dimming of the GFP-Rab5 fluorescence to background levels in

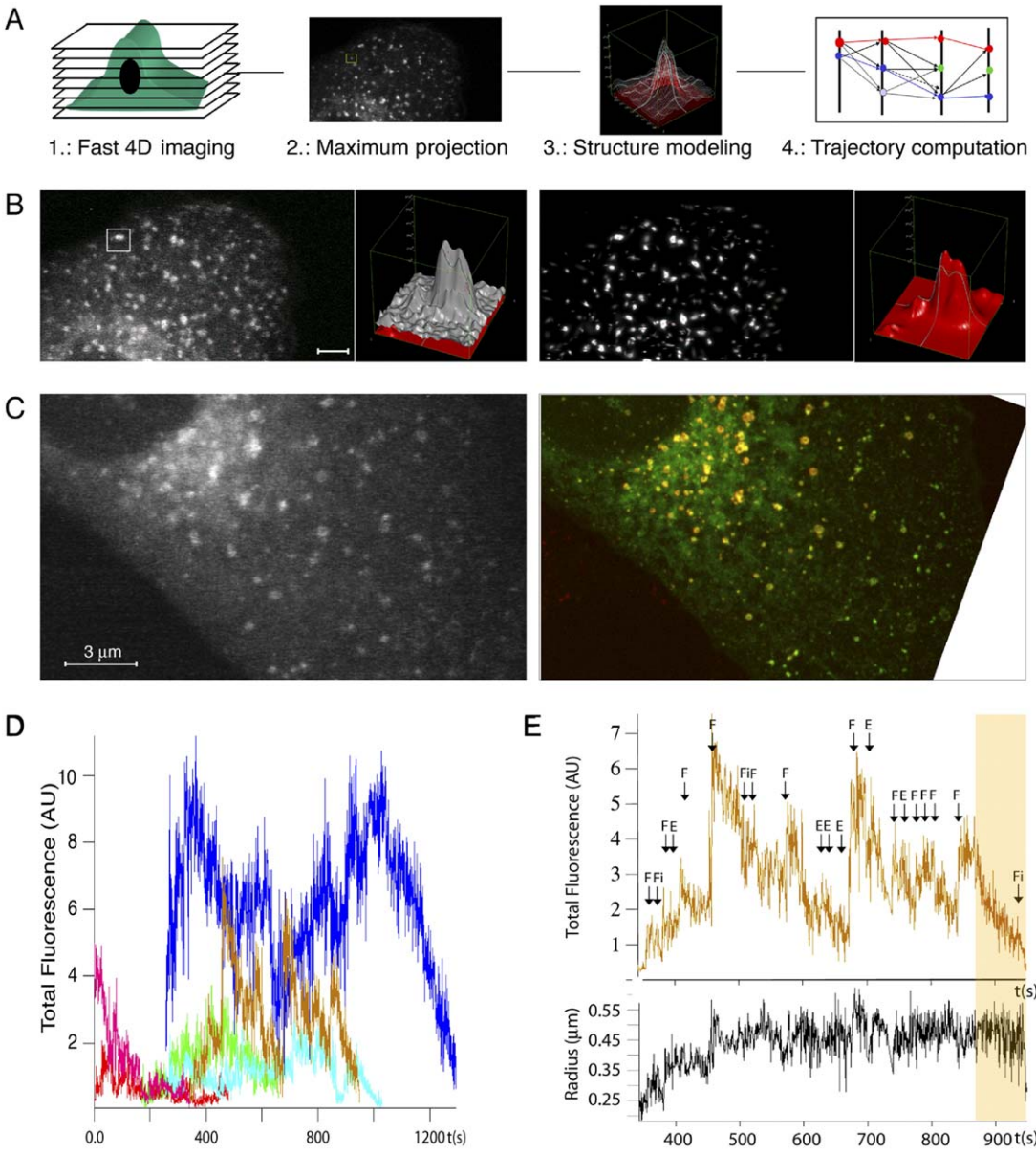

Figure 1. Dynamic Density Changes of Membrane-Associated Rab5 In Vivo

(A) Experimental setup for tracking of endosomes in living cells. (1) Fast 4D imaging at 8–10 frames/s at 37°C. (2) Collapse of individual Z stacks into one pseudo-3D image plane by maximum projection for subsequent processing (fluorescence intensity values were sufficiently preserved, as shown in Figure S1). (3) Computational modeling and quantification of endosomes. (4) Tracking of individual endosomes across the image sequence.

(B) Endosome identification and fitting by Motiontracking II. Most endosomes in the left panel (raw data) are recognized and modeled by the software (fitted image, right). The accuracy of modeling is illustrated by the asymmetric endosome boxed in the raw image. Left: measured intensity distribution within the boxed region (gray); right: modeled intensity distribution (red). Scale bar: 3 µm.

(C) Live-cell imaging was terminated by the perfusion of fixative into the imaging chamber, immunolabeling of the early-endosomal marker protein EEA1 was performed, and the cell featured in the live recording was located and imaged by high-resolution confocal laser scanning. Computational alignment of the resulting image (right: GFP-Rab5, green; EEA1, red) with the last frame of the live-cell sequence (left, GFP-Rab5 labeling only) shows that (1) most endosomes visualized by immunolabeling are also seen in the high-speed sequence and (2) most GFP-Rab5-bearing structures in the live-cell sequence are also positive for EEA1 (86% ± 0.5%, n = 3).

(D) GFP-Rab5 endosomes within a typical sequence (4 frames/Z stack, 2 stacks/s) were tracked automatically. Color-coded plots of total fluorescence-over-time traces of six representative endosomes are shown (see also Movie S1). All traces are characterized by strong fluctuations of associated Rab5 signal.

(E) Fusion events as major cause of fluctuations. One total fluorescence trace from Figure 1C (orange, top) is shown above the radius trace of the same endosome (black, bottom). Arrows denote the temporal position of F = fusion, E = encounter, and Fi = fission events. F was operationally defined as coalescence without subsequent fission, E as coalescence immediately followed by fission, and Fi as splitting of a previously stable structure (see also Movie S2). The yellow shading highlights the phase of terminal Rab5 loss from the structure.

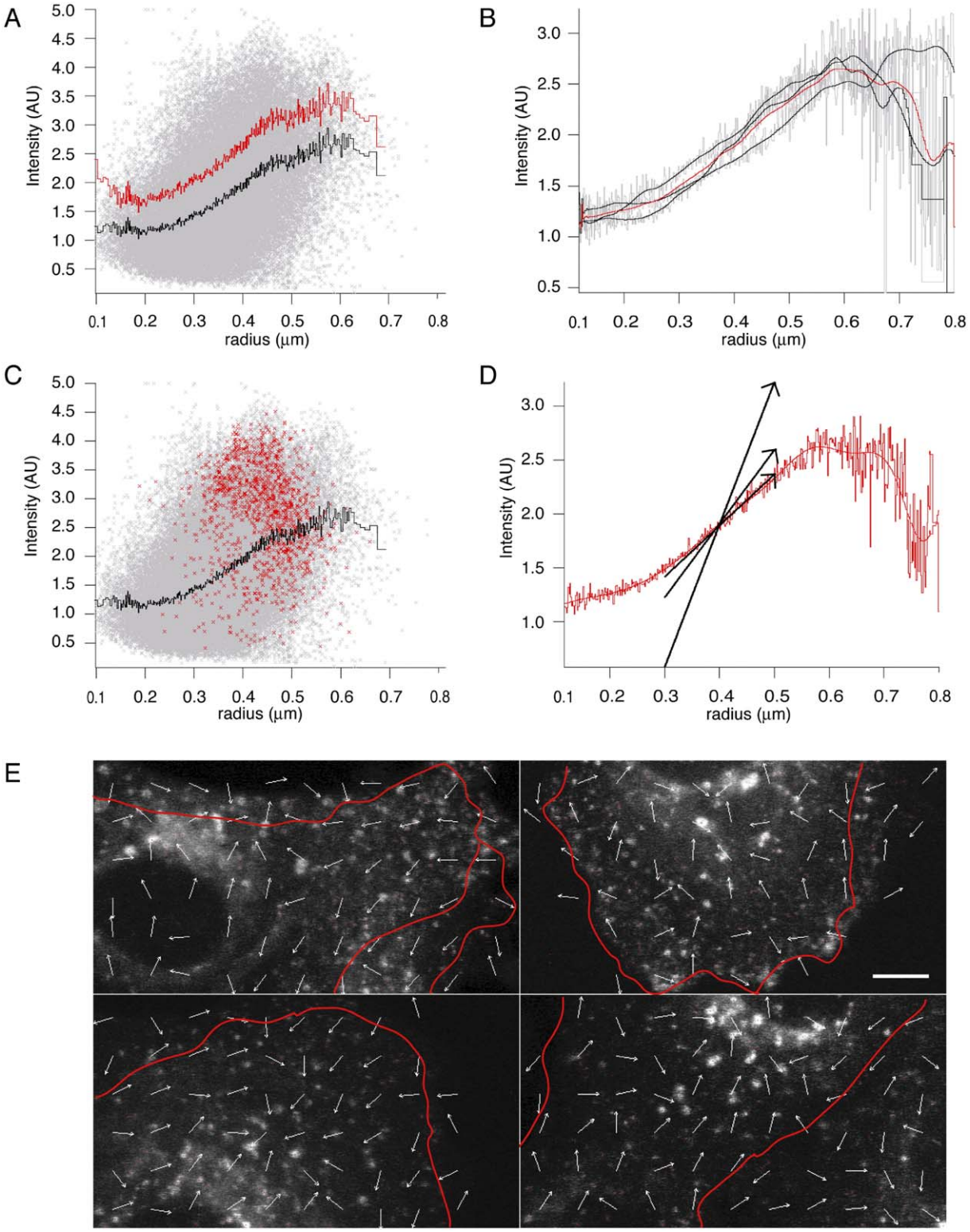

Figure 2. Global Analysis of Rab5 Endosome Dynamics

(A) Individual endosome measurements resulting from automated tracking of a typical GFP-Rab5 sequence (4 frames per Z stack, 2 stacks/s) were plotted as a 2D histogram according to their intensity (total fluorescence divided by 2× cross-sectional area) and radius (effective radius) values. The radius resolution limit in these experiments was experimentally determined to be 0.25 μm (see Experimental Procedures). The large number of individual measurements scatters into a broad cloud (gray). The positive slope of the trend line (black, representing the average intensity value of each radius bin) indicates increasingly intense Rab5 labeling with increasing endosome radius. Such positive slope is not an artifact of the systematic error in radius measurements, as the slope of the corrected trend line (red, shifted up for better visibility; see Figure S1F) is almost identical for structures above the resolution limit.

the trace presented in Figure 1E (top, shaded section). The radius of such structures clearly resolved by the microscope optics remained constant throughout the dimming process (Figure 2C, bottom), ruling out breakdown as trivial cause. We reproducibly observed such rapid fade-out events, although fusion was by far the predominant mode of track termination. Furthermore, fade-out events occurred most frequently among big, vacuole-like endosomes. Altogether, GFP-Rab5 is stably maintained on membranes over long periods of time but can, under certain circumstances, completely and irreversibly dissociate.

Population Dynamics of Rab5 Domains

Since fade-out events were observed comparatively rarely during the visual inspection of a small set of endosome tracks, we sought to confirm the reversible membrane association of the Rab5 machinery by a systematic population analysis of endosomes. Given that large endosomes appeared to preferentially undergo fade out, we first asked whether the surface density of GFP-Rab5 was in any way dependent on endosome size. We subjected the very large number of individual endosome measurements in a track set (typically 300,000/15 min sequence) to a histogram analysis of Rab5 fluorescence intensity (I, defined as total fluorescence/2× cross-sectional area) versus radius (R). The individual data points were widely scattered, as expected from the low signal-to-noise ratio of the image sequences and the fluctuations in the individual tracks (Figure 1D). Strikingly, however, the I/R plot revealed that the intensity of Rab5 labeling increased with the size of the structures and the magnitude of such increase far exceeded the systematic error inherent to optical radius measurements (Figure 2A and Figure S1F). Assuming that the majority of visible endosomes are individual structures and further approximating them to spherical vesicles, our data suggest that large endosomes generally have a higher Rab5 surface density than smaller endosomes. In the case of very large structures, however, this trend appeared to reverse again, although the significance of this observation was tempered by the low density of data points in this region of the histogram. Even though the correlation between endosome size and intensity is not deterministic, as indicated by the broad scattering of individual measurements, it is highly reproducible (Figure 2B).

The characteristic I/R relationship of GFP-Rab5 endosomes could reflect either a general progression from small and dim to large and bright structures or, alternatively, the existence of distinct, albeit partially overlapping, populations of endosomes with discrete I/R ratios. That the data points contributed by individual long tracks generally scattered over the entire width of the I/R diagram argued for the first hypothesis (Figure 2C). We next asked whether intensity or radius systematically change during the lifespan of endosomes. Interestingly, when examining large sets of tracks, we always detected a net increase of both I and R over the observation interval. The magnitude of the net change was always smaller than the SD of the measurement due to the large fluctuations and occasional fission events. Nevertheless, this result is significant. First, the standard error of the measurements was very small owing to the large data sets. Second, the net increases were independent of the length of the track fragments (between 50 and 600 frames). Third, all sequences examined invariably displayed a net increase in both I and R (Figure 2D). We therefore conclude that, on the whole, early endosomes grow in size and concomitantly increase the surface density of GFP-Rab5, thereby causing the characteristic shape of the I/R diagram.

Changes in Rab5 Dynamics Are Linked to the Movement of Early Endosomes

We next asked whether the population behavior of GFP-Rab5-positive endosomes was coordinated with endosome motility. When computationally analyzing the movement of all endosomes within a cell, we always detected net centripetal motility over most cellular areas (except for the cell edge, where rearrangements during cell locomotion interfere with the analysis; Figure 2E). The observed directionality is not a mere consequence of cell contraction since all cells analyzed actually expanded during the imaging. The directional component relative to total flow was small, consistent with the largely random movements at the single-endosome level. Thus, besides growing in I and R, endosomes also undergo a concomitant net movement from the cell periphery to the center. Since the directional changes were observed under steady-state conditions, one must deduce that Rab5 continuously redistributes from large structures in the cell center to small peripheral structures. The emergence of the latter is consistently visible in image sequences (Movie S3). The required loss of large structures is likely achieved by the fade-out events observed at the single-track level. This system analysis therefore strengthens our earlier con-

(B) Radius-intensity trend lines from three independent sequences (raw trend lines: gray; smoothened trend lines: black; average of smoothened trend lines: red). The close correspondence over the central regions indicates that the size-dependent intensity increase is a general feature of Rab5-positive endosomes. The divergence at large radius values is likely due to the low data densities in these regions (A).

(C) Highlighting of measurements from a manually verified track spanning 900 frames (red) within the total cloud of data points (gray) illustrates that individual endosomes can traverse the breadth of the radius-intensity diagram during their lifetime.

(D) The total set of tracks from three independent sequences was randomly fragmented into 100-frame segments. Average changes in intensity and radius over 100 frames were determined and visualized as radius-intensity vectors (arrows). Their positive slope demonstrates that, on average, both radius and intensity of individual endosomes increase over time.

(E) Population analysis of endosome movements. Four independent sequences, each spanning 13 min, were analyzed and tracked automatically. The image frame was subdivided into quadrants, and the net flow of tracked endosomes within quadrants was calculated. Arrows, superimposed on the last frame of the sequence, indicate the local direction of net flow over the entire observation interval. The nonrandom orientation of flow vectors indicates that, on average, Rab5 endosomes move toward the cell center. The outline of the cells at the start shown in red rules out contraction.

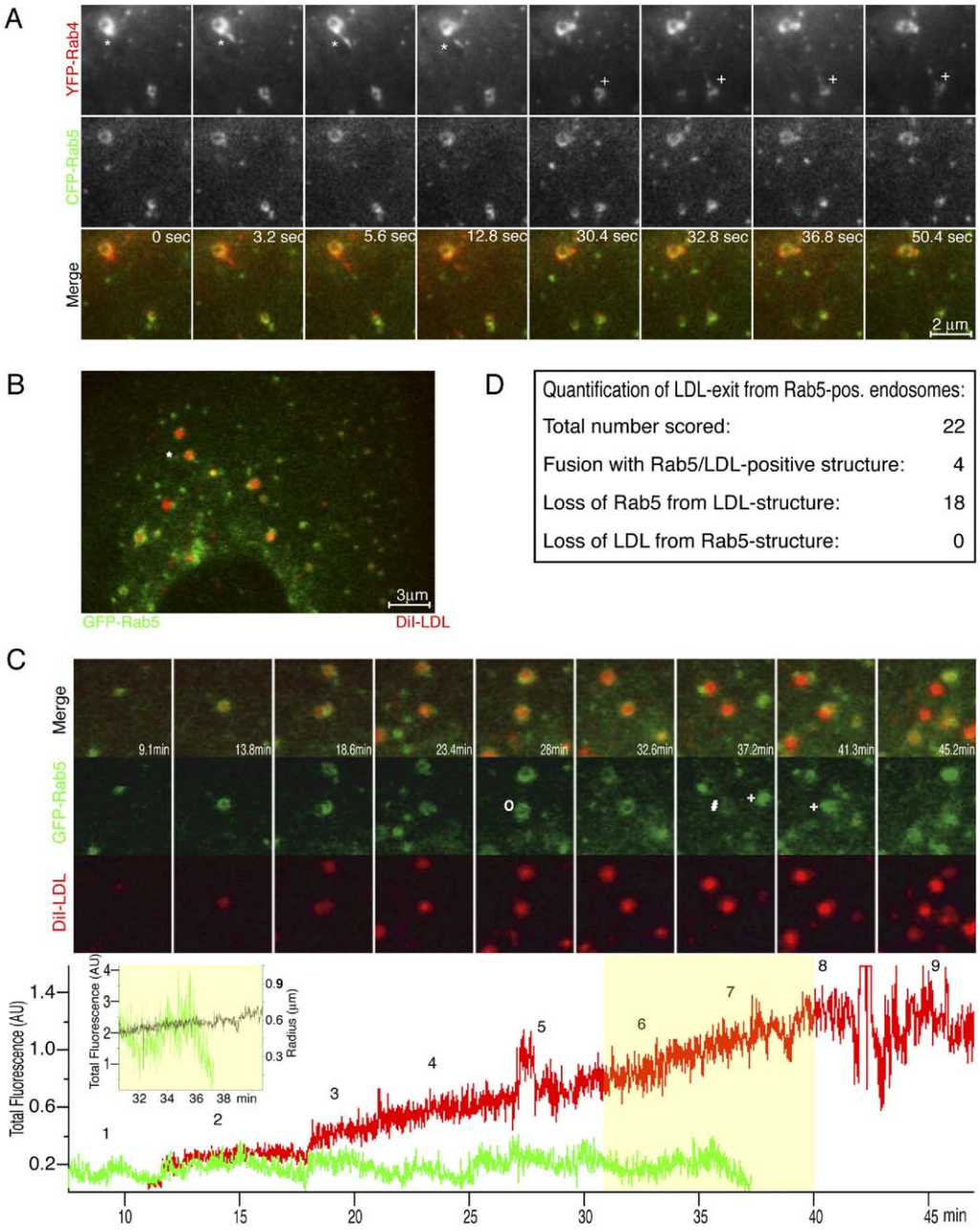

Figure 3. Cargo Exit from Rab5-Positive Structures

(A) A431 cells coinfected with adenoviruses expressing YFP-Rab4 (top) and CFP-Rab5 (middle; bottom: merge) 20 hr before the experiment were imaged at 37°C on an epifluorescence setup. Images were acquired at a frame rate of 1.2 Hz, with separate exposures for the two channels. * and + demarcate two independent events of Rab4-tubule outgrowth and fission from a Rab5-positive endosome. The stable GFP-Rab5 A431 cell line was imaged during the continuous uptake of DiI-LDL from the medium at 37°C. One four-frame/two-color Z stack/s was acquired for 40 min.

(B and C) A single frame out of a typical sequence is shown in (B) corresponding to 30 min. of DiI-LDL uptake. The white asterisk marks the endosome featured in (C) (top, approximate image center); the corresponding total fluorescence traces are shown below (Rab5: green; LDL: red). Inset: radius trace (black) of the LDL core and Rab5 total fluorescence trace (green) during Rab5 loss, throughout which the radius of the endosome remains nearly constant. Three morphological stages of Rab5 perimeter labeling are distinguished in the panel. °: full Rab5 perimeter labeling; #: Rab5 perimeter labeling dimmed almost to background levels shortly before completion of Rab5 loss; +: apparently restored Rab5 labeling is due to the temporal association of the LDL core with a separate endosome, previously tracked (+ label in 37.2 min frame).

(D) Quantification of LDL exit mode from Rab5-positive endosomes, based on 22 Rab5/LDL-positive structures randomly chosen from three independent sequences.

clusion that the Rab5 machinery is not indefinitely membrane associated.

Rab5 Dynamics during Cargo Transport through Early Endosomes

Loss of the Rab5 machinery from endosomal membranes may occur during the progression of cargo out of early endosomes. We therefore set up two-channel imaging protocols to visualize the dynamics of Rab5 in relation to markers of the recycling or degradative pathway (Rab4/Tf and Rab7/LDL, respectively). We observed the frequent outgrowth of Rab4-positive tubules from Rab5-positive endosomes (Figure 3A). Tf-containing tubules showed the same behavior (data not shown). Separation between Rab5 and Rab4 occurred by fission rather than loss of Rab5 (Figure 3A, Movie S4), likely reflecting the iterative removal of recycling cargo from early endosomes (Dunn et al., 1989; van der Sluijs et al., 1992; Sonnichsen et al., 2000; Ward et al., 2005). Next we investigated the possibility of Rab5 dissociation in conjunction with transport to late endosomes. Cells were allowed to internalize fluorescent LDL for 10 min prior to imaging. As expected, LDL entered GFP-Rab5-positive early endosomes, increasing almost linearly (Figures 3B and 3C). Small at first, LDL-positive endosomes gradually expanded, turning into vacuolar structures of ring-like morphology. Throughout, the Rab5 signal displayed the typical fluctuations described above (Figure 1D), which could again be mostly attributed to homotypic fusion with smaller Rab5 structures (data not shown).

Interestingly, the exit of LDL from early endosomes, as indicated by a loss of colocalization between LDL and Rab5, occurred through a relatively rapid fade out of the Rab5 signal around the perimeter of the LDL-structure (Figures 3C and 3D), suggestive of GDI-mediated extraction. Consistently, the R of the LDL core hardly changed throughout this process (inset, Figure 3C). However, recovery of minor amounts of Rab5 in budding events cannot be entirely ruled out. LDL structures that had just undergone GFP-Rab5 loss were often found to transiently associate with GFP-Rab5-bearing endosomes (Figure 3C) without, however, reestablishing Rab5 association along the full perimeter of the membrane. Therefore, such events likely represent peripheral interactions with distinct vesicles, also confirmed by careful visual inspection of the underlying movie sequences (Movie S5). Following loss of GFP-Rab5, LDL structures tended to be much more motile than Rab5-positive structures of comparable diameter and often tubulated and fused with similar Rab5-negative structures (Movie S6).

The sequence of events described above represents the general mode of transition from Rab5-positive to Rab5-negative membranes. First, the timescale of Rab5 turnover on cargo-bearing structures was in the range of the kinetics of transport along the degradative pathway (Dunn and Maxfield, 1992; Futter et al., 1996; Griffiths et al., 1989; Stoorvogel et al., 1991). Second, we systematically analyzed the loss of colocalization between LDL and Rab5 on 21 randomly chosen double-positive structures from three independent sequences (Figure 3D). All tracks eventually progressed to complete separation between Rab5 and LDL, which always occurred by Rab5 loss. We never observed a Rab5 structure to lose its LDL content. We cannot exclude the possibility that some LDL is also delivered to late endosomes by small carriers invisible in our experimental system. We find it unlikely since the high concentration of fluorescent LDL in the Rab5/LDL double-positive structures should allow the detection of even small budding vesicles.

Conversion from Rab5 to Rab7 during Early-to-Late-Endosome Transport

The above results raised the question of whether the loss of Rab5 was coordinated with the acquisition of Rab7. To visualize the dynamics of the two Rab proteins simultaneously, we constructed mRFP-tagged Rab5 and verified the functionality of the chimera as described above. Cells coexpressing mRFP-Rab5 and GFP-Rab7 were imaged during the continuous endocytosis of DiD-labeled LDL from the culture medium. LDL consistently accumulated in large, perinuclear mRFP-Rab5-positive endosomes (Figure 4A), which eventually lost Rab5. Remarkably, the Rab7 signal increased in parallel, resulting in conversion of the membrane perimeter from Rab5 positive/Rab7 negative to Rab5 negative/Rab7 positive (Figures 4B and 4C; Movie S7). Similar results were observed both under conditions of transient expression as well as in stable cell lines expressing the two tagged Rab proteins (data not shown).

We next addressed the temporal relationship between Rab conversion and the appearance of cargo in late endosomes by developing software for the quantitative analysis of high-resolution confocal images of fixed cells (Experimental Procedures). Late-endosomal compartments of stably GFP-Rab5-expressing cells were labeled by a 15 min pulse of DiI-LDL, followed by a 2.5 hr chase. Thereafter, a 10 min pulse of DiD-LDL was administered, and cells were fixed after suitable chase intervals. Twelve high-resolution confocal images were analyzed per time point, amounting to ~20,000 endosomes in 100 cells. Figure 5A shows that, after loss of the Rab5 machinery by conversion, cargo rapidly appeared in DiI-LDL-labeled late endosomes.

We noticed that, in contrast to lipid-core-labeled LDL (DiI- and DiD-LDL), the fluorescence signal of Alexa 405 fluorophores covalently linked to LDL surface proteins was rapidly lost after uptake. Such loss was strongly delayed by the microtubule-depolymerizing drug nocodazole (see Figure 5C), implying that it occurred upon transfer into a degradative compartment. We thus exploited this property to measure the kinetics of such transfer. Stably GFP-Rab5-expressing cells were pulsed with both DiD- and Alexa 405-LDL for 10 min and fixed after suitable chase intervals. Whereas the signal of DiD-LDL remained constant, the Alexa 405 signal decreased rapidly (Figure 5B). Interestingly, the decay kinetics were nearly identical to those of LDL exit from Rab5-positive compartments, indicating that, immediately after loss of the Rab5 machinery, cargo molecules encounter a degradative environment.

To verify that the removal of Rab5 is accompanied by the dissociation of its effector machinery and the subsequent acquisition of late-endosome features, we

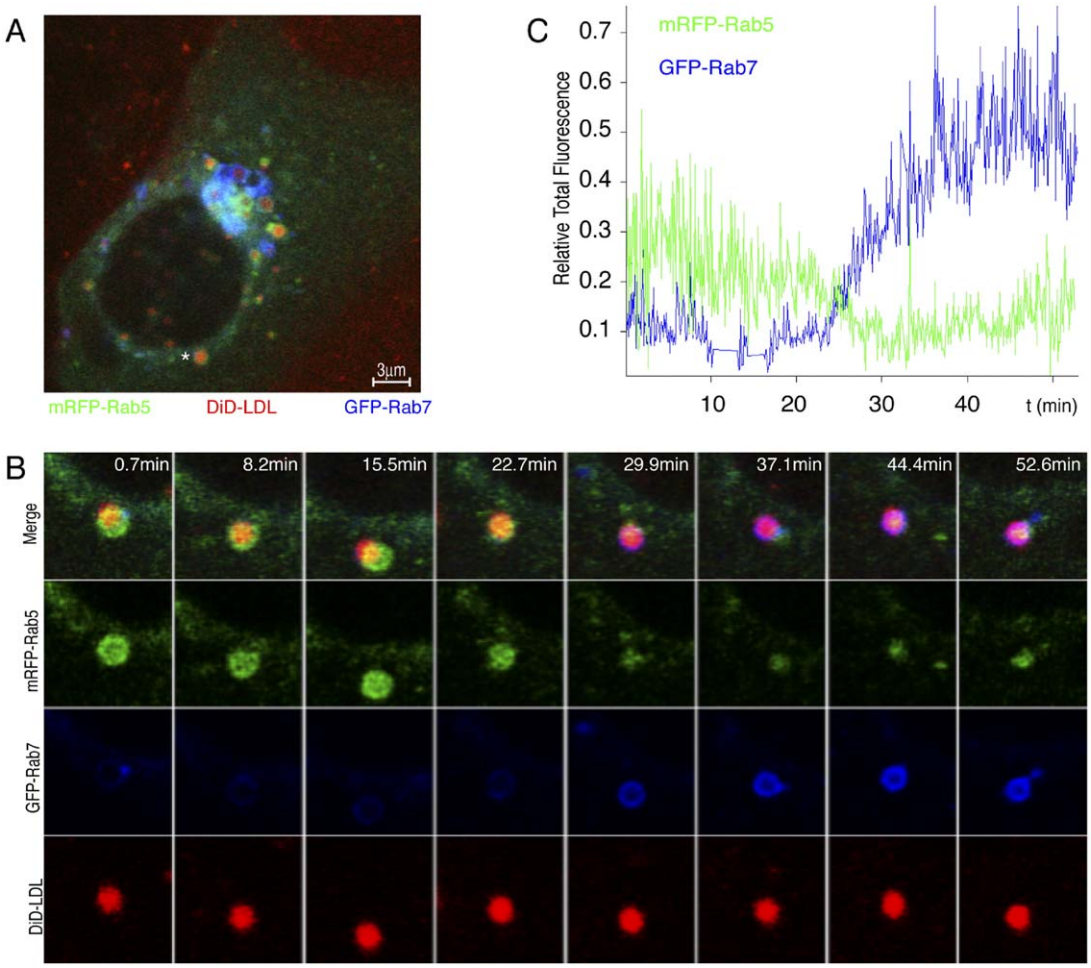

Figure 4. Endosomes Undergoing Rab5-to-Rab7 Conversion

Wild-type A431 cells transiently cotransfected with GFP-Rab7 and mRFP-Rab5 were imaged during the continuous uptake of DiD-LDL from the medium at 37°C for 60 min. One three-channel frame of a single focal plane was acquired every 4.6 s. Rab7 and DiD-LDL images were acquired simultaneously, mRFP-Rab5 in an independent scan (causing the color channel shift evident in [B]). A single frame out of a typical sequence is shown in (A) (color coding as indicated), corresponding to 30 min of DiD-LDL uptake. The asterisk marks the endosome featured in (B), depicted at the indicated times. The corresponding total fluorescence traces of Rab5 (green) and Rab7 (blue) are shown in (C). The traces were scaled to the DiD-LDL signal to smooth fluctuations caused by movements in and out of the acquisition plane.

measured the transit rates of LDL (10 min pulse) through GFP-Rab5-, EEA1-, or Lamp1-positive compartments by four-channel high-resolution confocal microscopy. Under control conditions (Figure 5C, top), the kinetics of LDL exit from Rab5- and EEA1-positive compartments again closely paralleled loss of the Alexa 405-LDL signal, demonstrating that Rab5 effectors dissociate from converting structures along with Rab5. Furthermore, the loss of Alexa 405 fluorescence occurs in Lamp1-positive compartments since (1) colocalization with Lamp1 increases rapidly at early time points, in agreement with Figure 5A, (2) Alexa 405-LDL is last detected in Lamp1-positive compartments, and (3) the total amount of LDL within the cell can at all times be largely accounted for by the two pools colocalizing either with EEA1 or Lamp1.

To kinetically resolve the processes between Rab conversion and appearance in late endosomes, we treated cells with 3 μM of nocodazole for 2 hr prior to the experiment. Under conditions of microtubule depolymerization (verified by immunofluorescence, data not shown), the Alexa 405-LDL signal was dramatically stabilized, suggesting that cargo transfer into degradative compartments was impaired (Figure 5C, bottom). Interestingly, the colocalization of LDL with Rab5 and EEA1 kept decreasing over time, consistent with ongoing egress from early endosomes. Live-cell-imaging experiments further confirmed that Rab conversion occurs without intact microtubules. However, the colocalization between LDL and Lamp1 was still found to increase over time, yet without the concomitant degradation of Alexa 405-LDL observed under control conditions. Therefore, microtubule depolymerization does not inhibit Rab conversion but likely a fusion step with a downstream hydrolytic compartment.

Regulation of Rab5-to-Rab7 Conversion

Finally, we addressed the molecular mechanisms underlying Rab5-to-Rab7 conversion. First, we examined the role of cargo destined for degradation. Given the

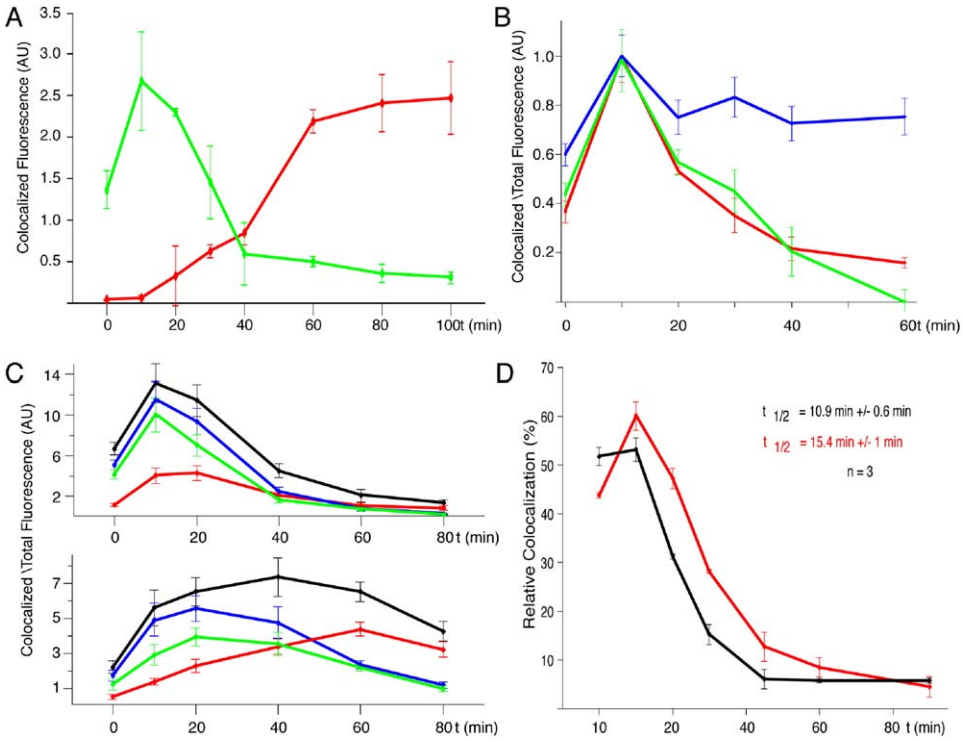

Figure 5. Rab Conversion and Transport to Late Endosomes

All traces are shown as mean values ± SD.

(A) Late endosomes in A431 cells stably expressing GFP-Rab5 and serum starved for 20 hr were labeled by a 15 min pulse of DiI-LDL and 2.5 hr chase in serum-free medium. Thereafter, a 10 min pulse of DiD-LDL was internalized, and cells were chased in serum-free medium for different periods of time, processed, and imaged by high-resolution confocal microscopy. Green: colocalization of DiD-LDL with GFP-Rab5 over time. Red: colocalization of DiD-LDL with DiI-LDL-labeled late endosomes over time.

(B) Cells were starved as in (A), labeled by internalization of a mix of DiD-LDL and Alexa 405-LDL for 10 min, chased in serum-free medium for different periods of time, processed, and imaged by high-resolution confocal microscopy. Blue: total DiD-LDL fluorescence. Green: total Alexa 405-fluorescence. Red: DiD-LDL fluorescence colocalizing with GFP-Rab5. Traces have been scaled to the same peak value.

(C) Cells starved as in (A) were either left untreated (control, top panel) or exposed to 3 μM nocodazole for the last 2 hr of serum starvation and all subsequent incubation steps (bottom). Following internalization of a 10 min pulse of Alexa 405-LDL, cells were chased in serum-free medium, fixed after the indicated chase intervals, immunostained, and imaged by high-resolution confocal microscopy. Total Alexa 405-LDL alone (black) or colocalizing with EEA1 (blue), Rab5 (green) or Lamp1 (red).

(D) A431 cells stably expressing GFP-Rab5 were serum starved for 20 hr. A 10 min pulse of DiD-LDL was internalized and mixed with either 1 μg/ml rhodamine-transferrin (control, black) or 200 ng/ml rhodamine-EGF (red). Cells were chased in serum-free medium, fixed after the indicated chase intervals, and imaged as above. Relative colocalization between LDL and GFP-Rab5 over time is shown. Mean half-time values (±SD) under control and EGF conditions were derived from three independent experiments by fitting the decay phase of the traces with single exponentials.

reported interaction between activated EGFR and regulators of the Rab5 cycle (Di Fiore and De Camilli, 2001), we tested the effect of epidermal growth factor (EGF) on LDL-transit rates through early endosomes. Cells were serum starved for 20 hr, pulsed for 10 min with DiD-LDL either mixed with 5 μg/ml rhodamine-Tf (control) or 200 ng/ml rhodamine-EGF, and chased in serum-free medium. Interestingly, LDL transit was slower in the presence of EGF (Figure 5D). Fitting of the exponential decay phase of the curves yielded estimates of transit half-times of 10.9 ± 0.6 min under control conditions and 15.4 ± 1 min in the presence of EGF (n = 3). As the decay parameters of control and EGF curves differed, we can rule out that the delay is caused by a curve shift due to delayed LDL uptake. These data show that EGFR activation not only stimulates endocytosis via activation of Rab5 (Di Fiore and De Camilli, 2001) but also exerts a negative effect on early-to-late-endosomal transport.

Rab conversion depends on the ability of Rab5 to hydrolyze GTP, allowing its extraction from the membrane. Consequently, a Rab5 mutant defective in GTP hydrolysis would be expected to result in endosomes that recruit Rab7 but fail to displace Rab5. We tested this by examining the effects of the GTPase-deficient $Rab5^{Q79L}$ mutant (Stenmark et al., 1994). In contrast to wt Rab5 (Figure 4A and data not shown), $Rab5^{Q79L}$ induced a striking recruitment of Rab7 onto the expanded endosomes (Figure 6A). EEA1 and Lamp1 also colocalized on the vacuoles (data not shown).

Altogether, these observations suggest the existence of a molecular link between the Rab5 and Rab7 machineries. Analysis of the Rab5-interacting molecules identified by affinity chromatography from HeLa cell cytosol (Christoforidis et al., 1999) provided an important clue into such a mechanism. Among the proteins specifically interacting with GST-Rab5:GTPγS, hVps11 was identified by mass spectrometry (MS) sequencing (Fig-

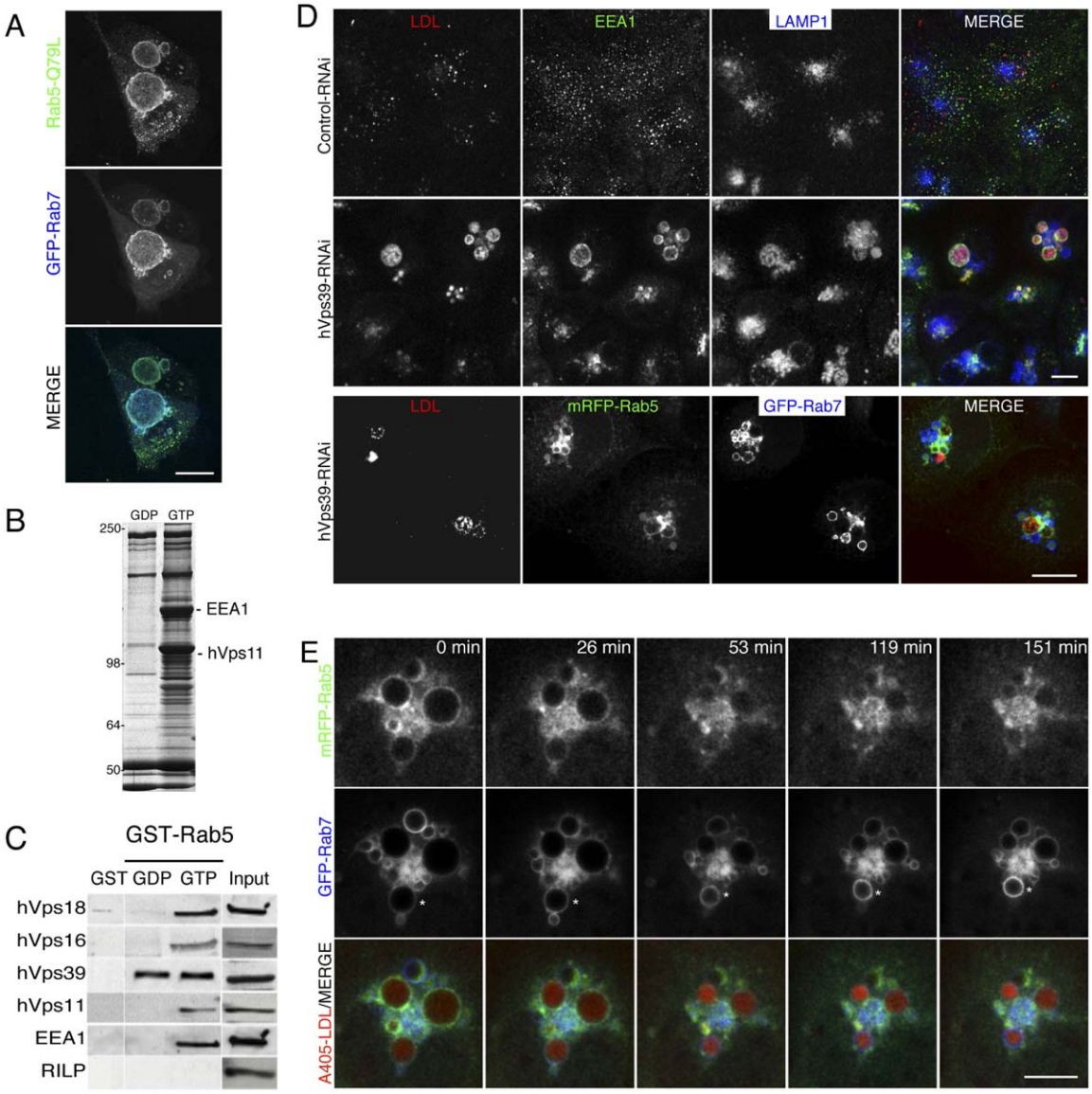

Figure 6. Molecular Mechanism of Rab5-to-Rab7 Conversion

All scale bars: 10 μm.

(A) A431 cells cotransfected with the GTP-hydrolysis-deficient Rab5 mutant Q79L and GFP-Rab7 were fixed, processed for immunofluorescence, and imaged by confocal microscopy. A maximum-projected Z stack is shown.

(B) Silver-stained gel of Rab5 effectors isolated from HeLa cytosol by affinity chromatography with GDP (left) or GTPγS (right) loaded GST-Rab5. The bands corresponding to EEA1 and hVps11 are indicated.

(C) Rab5-column eluates were probed with anti-hVps18, -hVps16, -hVps39, -hVps11, and -EEA1 (positive control) and anti-RILP (negative control) antibodies. Input: HeLa cytosol.

(D) Effects of hVps39 knockdown. A431 cells were transfected either with control (top) or anti-hVps39 siRNA (as indicated) and grown for 72 hr, the last 20 hr thereof in serum-free medium. A 10 min pulse of Alexa 405-LDL was internalized, and the cells were chased in serum-free medium, fixed, immunostained for the indicated markers, and imaged by confocal microscopy. To visualize Rab5 and Rab7, the cells shown in row 3 were coinfected with adenoviruses expressing GFP-Rab7 or mRFP-Rab5 12 hr before the LDL uptake. The top two rows show cells after 30 min of chase; the third row shows cells after 90 min of chase.

(E) A431 cells were transfected with anti-hVps39 siRNA as above. Twelve hours prior to the experiment, cells were coinfected with adenoviruses expressing mRFP-Rab5 and GFP-Rab7. A 10 min pulse of Alexa 405-LDL was internalized, and the coverslips were mounted in serum-free medium. Live-cell imaging was carried out at 37°C, and single three-channel optical sections were acquired every 10 s.

ure 6B). Vps11 is one of six subunits of the class C VPS/HOPS complex (Rieder and Emr, 1997; Seals et al., 2000), highly conserved from yeast to man (Caplan et al., 2001; Kim et al., 2001; Richardson et al., 2004). The presence of the class C VPS/HOPS complex was confirmed by Western blot. All four subunits for which antibodies were available (Richardson et al., 2004) could be detected in the GST-Rab5-column eluate (Figure 6C).

Similar pull-down experiments with GST-Rab7 confirmed the expected Rab7-class C VPS/HOPS interaction in mammalian cells (data not shown).

Importantly, the Vps39p subunit of class C VPS/HOPS has been shown to have GEF activity toward Ypt7p, the *S. cerevisiae* Rab7 ortholog. These data are consistent with an involvement of the complex in the Rab5-dependent recruitment of Rab7 onto endosomes about to undergo conversion. Accordingly, impeding the function of the class C VPS/HOPS complex should lead to delayed conversion. We therefore set up conditions to knock down hVps39 by RNAi as determined by RT-PCR (Supplemental Data). Treatment of A431 cells with anti-hVps39, but not control siRNA, led to a striking enlargement of EEA1/Rab5-positive early endosomes and Lamp1/Rab7-positive late endosomes (Figure 6D), a phenotype partially mimicked by the knockdown of other subunits of the class C VPS/HOPS complex (Vps16, data not shown). These phenotypic alterations are consistent with a delayed recruitment/activation of Rab7 onto the Rab5-positive early endosomes that consequently grow beyond their normal size (Figure 2A). Although early- and late-endosomal markers remained mostly segregated, occasionally vacuoles positive for both could be observed. Importantly, although the EEA1/Rab5-positive vacuoles were still accessible to 10 min pulses of endocytosed Alexa 405-LDL, the exit kinetics of LDL were dramatically reduced relative to control conditions (Figure 6D). After 90 min of chase, the majority of LDL still resided in EEA1-positive compartments, and colocalization between LDL and EEA1 persisted for up to 4 hr (data not shown). Alexa 405-LDL could eventually be observed within enlarged Lamp1/Rab7-positive vacuoles, suggesting that the latter arise from EEA1/Rab5-positive vacuoles by conversion. This hypothesis could indeed be confirmed by live-cell imaging under hVps39 depletion. However, in stark contrast to basal conditions, the kinetics of conversion shifted from a timescale of minutes to hours. The endosome labeled by an asterisk in Figure 6E exemplifies such gradual increase of Rab7 and concomitant decrease of Rab5 labeling over a 2.5 hr interval. The greatly reduced conversion kinetics further provide an explanation for the vacuoles double-positive for early (EEA1/Rab5) and late (Lamp1/Rab7) endosomal markers occasionally observed under hVps39 knockdown. Altogether, these results implicate the class C VPS/HOPS complex in the Rab5-dependent recruitment of Rab7 onto endosomes.

Discussion

Rab proteins are a central element of the trafficking machinery and are of strategic importance in the determination of organelle identity (Pfeffer, 2001; Zerial and McBride, 2001). Their dynamics are largely unexplored in vivo, especially in the course of intracellular transport. Here, we developed a quantitative live-cell-imaging approach to analyze the dynamics of Rab5-positive early endosomes and the transfer of cargo to Rab7-positive late endosomes. Our experiments led to three key findings. First, the level of Rab5 dynamically fluctuates on individual early endosomes, which by fusion and fission events are linked into a network in time. Second, through repetitive fusion events, degradative cargo becomes highly enriched in progressively fewer and larger endosomes, which are rapidly removed from the early-endosomal network in the cell center via the loss of Rab5 and the concomitant acquisition of Rab7. Third, this conversion requires the class C VPS/HOPS complex, an established Rab7 GEF, which we found to interact with Rab5. These results establish a mechanistic paradigm for the remodeling of membrane identity via the coordinated exchange of Rab machineries.

Dynamic Association of Rab5 with an Early-Endosomal Network

Our data allow us to formulate a model whereby dynamic association and dissociation of Rab GTPases are key aspects of endosome biogenesis and maintenance, as well as cargo progression along the endocytic pathway (Figure 7). An important finding is that the association of Rab5 with early endosomes is much more dynamic than expected. Rab5 levels on individual endosomes fluctuate constantly, rapidly relaxing back to a steady-state level after the frequent increments upon homotypic fusion events. Due to such high frequency of homotypic fusion events (Figure 2), early endosomes can no longer be considered as individual entities but rather comprise a network in time. This behavior is part of a functional cycle where Rab5-positive endosomes are constantly generated/renewed in the cell periphery and move toward the cell center while growing in size. The cyclical assembly/disassembly of the Rab5 machinery confers dynamic properties to early endosomes ranging between two extremes: they can either be stably maintained over several minutes or, alternatively, undergo rapid loss of their early-endosomal identity in conversion events.

All endosomes receive incoming vesicles from the plasma membrane. Recycling cargo exits in Rab4-positive tubules, which frequently grow out and detach from Rab5-positive cores, consistent with constant nucleation of Rab4 domains. Cargo destined for late endosomes is retained in individual endosomal units. Thus, by the parallel sorting activities and interconnectivity of endosomes, degradative cargo gradually accumulates in fewer and bigger endosomes. Although homotypic fusion events can temporarily restore Rab5 levels, Rab conversion eventually occurs on such structures, causing their rapid removal from the early-endosomal network and rendering them fusion competent with late endosomes. The early- and late-endosomal systems are thus kept largely separated, connected only by the sparse one-way connections of conversion events. As these are rare at steady state, Rab5-positive membranes undergo comparatively slow turnover with half-lifes of 10–15 min, remarkably consistent with the reported kinetics of transport from early to late endosomes (Futter et al., 1996; Salzman and Maxfield, 1989; Stoorvogel et al., 1991; Griffiths et al., 1989). Conversion is instrumental to the integrity of the endosomal network, as it also allows the recycling of Rab5 onto nascent endosomes in the cell periphery. Recycling is most likely mediated by Rab-GDI, but some Rab5 may also be recovered from converting structures in bud-

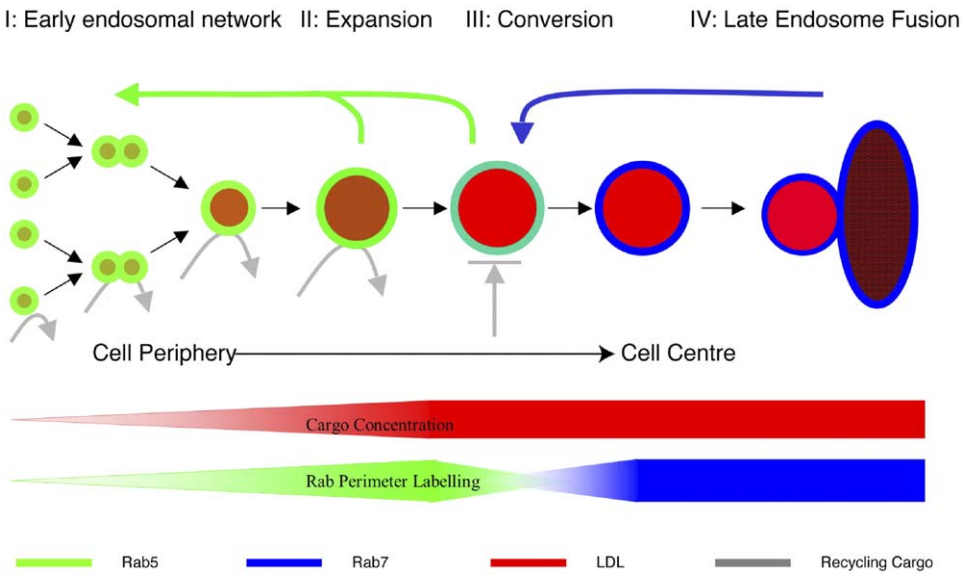

Figure 7. Model Depicting Rab5 and Early-Endosome Dynamics

The network properties of early endosomes are symbolized on the left. The transient colocalization of Rab5 and Rab7 during conversion is illustrated by cyan color; hatching represents degradative late endosomes. Green arrows show recycling of dissociated Rab5 back onto peripheral endosomes; blue arrows show the recruitment of Rab7 onto converting endosomes. Gray arrows represent fusion of cargo vesicles and subsequent recycling. The bars at the bottom depict the dynamic processes occurring concomitantly with centripetal translocation: Red: gradual accumulation and concentration of LDL. Green: gradual accumulation of Rab5, followed by conversion to Rab7. See text for detailed discussion.

ding events below the detection limits of our techniques.

Rab Domains Undergo Assembly and Disassembly

Rab GTPases organize the endocytic pathway into a mosaic of biochemically and functionally distinct membrane domains (Barbero et al., 2002; Sonnichsen et al., 2000). Our present observations suggest that Rab domains are not maintained indefinitely but can be disassembled. These dynamics are controlled by the nucleotide cycle of Rab GTPases, as it determines the association and dissociation of Rab GTPases from the membrane. Such coupling to the GTP-free energy gradient maintains Rab domains in a metastable state, allowing for rapid and complete disassembly. Given the large number of Rab effectors (Zerial and McBride, 2001), exchange of the resident Rab GTPases alone entails the release of a much greater number of peripheral membrane proteins. Rab GTPases therefore seem to have evolved as strategic switches to rapidly remodel membranes. They are uniquely tailored to such a dynamic system: SNAREs, for example, are integral membrane proteins that cannot be extracted from the membrane, entailing a much broader distribution between compartments and thus a diminished utility as compartment identity cues.

We further found that cargo modulates the kinetics of transport between early and late endosomes. EGF slows the transport of LDL through early endosomes by 50%. This effect can be explained by the increased GTP loading of Rab5 in response to activated EGFR (Di Fiore and De Camilli, 2001). A higher ratio of GTP versus GDP bound Rab5 would be expected to retard the loss of Rab5 from cargo-bearing membranes, as observed with the $Rab5^{Q79L}$ mutant. Such cargo dependence may be a general feature of this transport route, given the importance of cargo concentration in the overall efficiency of transport by Rab conversion. An interesting conclusion from our study is that activated growth-factor receptors may actively exploit such cargo dependence in order to modulate the extent of their downstream signaling processes.

Molecular Mechanism of Rab Conversion

In light of our findings, the distinct protein composition of early and late endosomes demonstrated by Schmid et al. (1988) can thus be expected to result, at least in part, from the exchange of Rab5 for Rab7 at the interface between early and late endosomes. We could further demonstrate that this transition is regulated by the class C VPS/HOPS complex (Price et al., 2000; Rieder and Emr, 1997), which we here found to interact with Rab5:GTP. Since the Vps39p subunit of class C VPS/HOPS has GEF activity on Ypt7p (Wurmser et al., 2000), the yeast ortholog of Rab7, the coupling between Rab5 and activation of Rab7 is remarkably similar to the sequential activation of Ypt31/32p and Sec4p in the yeast secretory pathway (Ortiz et al., 2002). Ypt31/32p has been shown to recruit Sec2p, leading to the activation of Sec4p on secretory vesicles. However, whereas Sec2p has been interpreted to link the function of Ypt31/32p in vesicle budding with the function of Sec4p in vesicle targeting, the mechanism here described is used instead to reprogram the molecular identity of a compart-

ment as a means of cargo transport. Consistently, we found that RNAi-mediated knockdown of the hVps39 subunit caused a striking enlargement of both early and late endosomes. The Rab5-positive vacuoles accumulated internalized cargo over many hours, providing a likely explanation for their gross enlargement. These vacuoles eventually acquired Rab7, but with kinetics in the range of hours rather than minutes. These results are consistent with a rate-limiting function of the class C VPS/HOPS complex in the recruitment of Rab7 during conversion. This complex likely exerts a range of functions in trafficking, including tethering/fusion to late endosomes/lysosomes (Caplan et al., 2001; Poupon et al., 2003; Price et al., 2000; Rieder and Emr, 1997). However, it appears unlikely that the observed phenotype is due to an impairment of the latter activity, as fragmented rather than enlarged endosomes would be expected. Moreover, localization data in mammalian cells (Kim et al., 2001; Richardson et al., 2004) as well as functional studies in *S. cerevisiae* (Peterson and Emr, 2001) are consistent with the proposed function at the interface between early and late endosomes. Following the class C VPS/HOPS-dependent recruitment of Rab7 onto Rab5-positive endosomes, the completion of conversion likely involves negative feedback between the Rab7 and Rab5 domains, which could possibly be exerted via a Rab5-GAP amongst the Rab7 effectors.

Relationship to Existing Models

Our data has the benefit of reconciling mechanistic aspects of both the maturation and vesicle-transport models of the endocytic pathway (Griffiths and Gruenberg, 1991; Murphy, 1991). Overall, the process of conversion can be related to the endosomal carrier vesicle (ECV) model described by Gruenberg et al. (1989). Although originally proposed to bud from early endosomes, we now suggest that these 400–800 nm vesicles arise from early endosomes by conversion from Rab5 to Rab7, based on the following observations. First, whereas Rab5 is depleted from ECV-enriched fractions (Aniento et al., 1993), at least exogenously expressed Rab7 can be detected in such preparations (J. Gruenberg, personal communication), consistent with Rab conversion. Second, ECVs have been isolated from nocodazole-treated cells, where conversion still takes place. Third, the nocodazole-induced accumulation of ECVs has been attributed to impaired fusion with late-endosomal compartments, consistent with the lack of Alexa 405-LDL degradation under these conditions. As individual endosomes have a much greater probability of being consumed in homotypic fusion events than undergoing conversion, early endosomes can be seen as the stable compartment evoked previously (Griffiths and Gruenberg, 1991). On the other hand, the infrequent conversion events are consistent with maturation models of endosomal transport (Murphy, 1991). Further, the progressive density shift of early-endosomal fractions detected (Stoorvogel et al., 1991) and the 30 min period of EGF accumulation by individual endosomes (Futter et al., 1996) can likely be attributed to the gradual convergence of cargo in fewer and bigger structures prior to conversion.

Overall, therefore, our results provide a novel view of endosomal transport, in which the global dynamics of an endosomal network are intimately linked to the local dynamics of Rab GTPases on individual organelles. Such a view emerged from the development and application of novel tools allowing the quantitative analysis of endosomal transport in living cells. Our study thus paves the way toward a system-biology-analysis approach to this essential cellular process.

Experimental Procedures

For details on cell culture, transfection, DNA constructs, antibodies, LDL labeling and uptake, and RNA interference, see Supplemental Data.

Imaging

For high-resolution imaging of fixed cells, coverslips were mounted in Mowiol and imaged on an inverted LSM510 confocal laser scanning microscope (Carl Zeiss). Twelve bit images were acquired through Plan-Apochromat objectives under zoom settings of 1, scan speed 7, averaging 2, and pinhole settings resulting in 0.8 μm Z sections. Epifluorescence live-cell imaging was carried out as described (Sonnichsen et al., 2000). For fast confocal live-cell imaging, coverslips were mounted in normal growth medium in a closed chamber with internal temperature control (Harvard Apparatus). All imaging was carried out at 37°C on an inverted LSM510 confocal laser scanning microscope (Carl Zeiss) equipped with a heated 40×/1.2 W C-Apochromat objective and a piezo-driven Z stage. Sequences were acquired as 12 bit 512/300 image frames, using 3 μm optical sections and bidirectional scanning at speeds 12 or 13. Three to four Z planes were acquired per time point. Multitrack protocols utilizing bidirectional scanning and "switch between lines" were used for fast multichannel imaging. Z stacks were collapsed by maximum projection and exported as 16 bit TIF sequences for further analysis. The radius resolution limit was taken as the peak of the radius distribution of processed image sequences of green fluorescent 170 nm beads (Molecular Probes) in aqueous suspension.

Image Analysis

All image processing and analysis was carried out with the Motiontracking II program:

Image Fitting

Following background subtraction by windowed floating mean, fluorescent structures in the images were modeled by:

$$I(x,y) = \sum_i \frac{A_i}{1 + \left\{ \left[\frac{(x - x_i)\cos(\alpha_i) - (y - y_i)\sin(\alpha_i)}{w_i} \right]^2 + \left[\frac{(x - x_i)\sin(\alpha_i) + (y - y_i)\cos(\alpha_i)}{h_i} \right]^2 \right\}^2} + B(x_i, y_i)$$

where A_i = intensity; x_i, y_i = center coordinates; w_i, h_i = width by two perpendicular dimensions; α_i = angle between main axes and x/y image axes, B(x_i, y_i) = background residue in the vicinity of the particle; and index i refers to the i^{th} particle.

Fitted structures were subtracted from the image, and the procedure was repeated iteratively to capture all structures above two SD of noise. Two partially overlapping peaks were combined if the ratio between peak height and local minimum did not exceed 50%. Image fitting produced a particle set with known position, cross-sectional area, and total fluorescence, serving as basis for all further calculations.

Vesicle Tracking

The algorithm was developed as generalization of the Hungarian algorithm, assigning four consecutive image frames at once with track breaks as assignment possibility and essentially overcoming the use of greedy algorithms. Track assignments were made on basis of the weighted sum of scores for position, speed, cross-sectional area, maximum intensity, total vesicle fluorescence, and

termination penalty, calculated according to Verestoy et al. (1999). Weights were manually adjusted.

Net-Flow Analysis

The image frame was divided into square cells, in which flow was calculated as sum $F=\Sigma I_i \cdot v_i$, where I_i = the integral intensity of i^{th} vesicle and v_i = the speed of i^{th} vesicle, which included all vesicle tracks of the image sequences.

Colocalization Analysis

Colocalization was assessed on basis of cross-sectional overlap, scoring >50% overlap as colocalized. Colocalized fluorescence was calculated as the sum of integral fluorescence intensities of all colocalized vesicles. Fluorescence measurements were standardized to cell area by the ratio of "masked" area to the total frame area. The mask was calculated by extreme smoothing ($\sigma \sim 1\ \mu m$) and subsequent threshold cutoff on the basis of the GFP-Rab5 background fluorescence.

Supplemental Data

Supplemental Data include Supplemental Experimental Procedures, two figures, and seven movies and can be found with this article online at http://www.cell.com/cgi/content/full/122/5/735/DC1/.

Acknowledgments

We are indebted to Dr. R. Piper and Dr. J. Neevjes for providing antisera against class C VPS/HOPS components and RILP, respectively; Dr. J. Cohen for GFP-rotavirus-like particles; and Dr. R. Tsien for mRFP-cDNA. We would further like to thank R. Schaefer for expert technical assistance; Dr. O. Vieira for advice on preparation of LDL; and Drs. M. Miaczynska, K. Simons, J. Howard, K. Khairy, B. Hoflack, L. Pelkmans, and A. Schenck for critical reading of the manuscript. This work was supported by grants from the HFSP (RG-0260/1999-M), the European Union (HPRN-CT-2000-00081), and the Max Planck Society.

Received: August 30, 2004
Revised: May 10, 2005
Accepted: June 24, 2005
Published: September 8, 2005

References

Aniento, F., Emans, N., Griffiths, G., and Gruenberg, J. (1993). Cytoplasmic dynein-dependent vesicular transport from early to late endosomes. J. Cell Biol. *123*, 1373–1387.

Barbero, P., Bittova, L., and Pfeffer, S.R. (2002). Visualization of Rab9-mediated vesicle transport from endosomes to the trans-Golgi in living cells. J. Cell Biol. *156*, 511–518. Published online February 4, 2002. 10.1083/jcb.200109030.

Bock, J.B., Matern, H.T., Peden, A.A., and Scheller, R.H. (2001). A genomic perspective on membrane compartment organization. Nature *409*, 839–841.

Caplan, S., Hartnell, L.M., Aguilar, R.C., Naslavsky, N., and Bonifacino, J.S. (2001). Human Vam6p promotes lysosome clustering and fusion in vivo. J. Cell Biol. *154*, 109–122.

Charpilienne, A., Nejmeddine, M., Berois, M., Parez, N., Neumann, E., Hewat, E., Trugnan, G., and Cohen, J. (2001). Individual rotavirus-like particles containing 120 molecules of fluorescent protein are visible in living cells. J. Biol. Chem. *276*, 29361–29367. Published online May 16, 2001. 10.1074/jbc.M101935200.

Christoforidis, S., McBride, H.M., Burgoyne, R.D., and Zerial, M. (1999). The Rab5 effector EEA1 is a core component of endosome docking. Nature *397*, 621–625.

Conner, S.D., and Schmid, S.L. (2003). Regulated portals of entry into the cell. Nature *422*, 37–44.

Di Fiore, P.P., and De Camilli, P. (2001). Endocytosis and signaling. an inseparable partnership. Cell *106*, 1–4.

Dunn, K.W., and Maxfield, F.R. (1992). Delivery of ligands from sorting endosomes to late endosomes occurs by maturation of sorting endosomes. J. Cell Biol. *117*, 301–310.

Dunn, K.W., McGraw, T.E., and Maxfield, F.R. (1989). Iterative fractionation of recycling receptors from lysosomally destined ligands in an early sorting endosome. J. Cell Biol. *109*, 3303–3314.

Futter, C.E., Pearse, A., Hewlett, L.J., and Hopkins, C.R. (1996). Multivesicular endosomes containing internalized EGF-EGF receptor complexes mature and then fuse directly with lysosomes. J. Cell Biol. *132*, 1011–1023.

Gasman, S., Kalaidzidis, Y., and Zerial, M. (2003). RhoD regulates endosome dynamics through Diaphanous-related Formin and Src tyrosine kinase. Nat. Cell Biol. *5*, 195–204.

Geuze, H.J., Stoorvogel, W., Strous, G.J., Slot, J.W., Bleekemolen, J.E., and Mellman, I. (1988). Sorting of mannose 6-phosphate receptors and lysosomal membrane proteins in endocytic vesicles. J. Cell Biol. *107*, 2491–2501.

Griffiths, G., and Gruenberg, J. (1991). The arguments for pre-existing early and late endosomes. Trends Cell Biol. *1*, 5–9.

Griffiths, G., Back, R., and Marsh, M. (1989). A quantitative analysis of the endocytic pathway in baby hamster kidney cells. J. Cell Biol. *109*, 2703–2720.

Gruenberg, J., and Maxfield, F.R. (1995). Membrane transport in the endocytic pathway. Curr. Opin. Cell Biol. *7*, 552–563.

Gruenberg, J., Griffiths, G., and Howell, K.E. (1989). Characterization of the early endosome and putative endocytic carrier vesicles in vivo and with an assay of vesicle fusion in vitro. J. Cell Biol. *108*, 1301–1316.

Helenius, A., Mellman, I., Wall, D.A., and Hubbard, A. (1983). Endosomes. Trends Biochem. Sci. *8*, 245–250.

Henry, R.M., Hoppe, A.D., Joshi, N., and Swanson, J.A. (2004). The uniformity of phagosome maturation in macrophages. J. Cell Biol. *164*, 185–194.

Kim, B.Y., Kramer, H., Yamamoto, A., Kominami, E., Kohsaka, S., and Akazawa, C. (2001). Molecular characterization of mammalian homologues of class C Vps proteins that interact with syntaxin-7. J. Biol. Chem. *276*, 29393–29402. Published online May 29, 2001. 10.1074/jbc.M101778200.

McBride, H.M., Rybin, V., Murphy, C., Giner, A., Teasdale, R., and Zerial, M. (1999). Oligomeric complexes link Rab5 effectors with NSF and drive membrane fusion via interactions between EEA1 and syntaxin *13*. Cell *98*, 377–386.

Mellman, I. (1996). Endocytosis and molecular sorting. Annu. Rev. Cell Dev. Biol. *12*, 575–625.

Murphy, R.F. (1991). Maturation models for endosome and lysosome biogenesis. Trends Cell Biol. *1*, 77–82.

Nielsen, E., Severin, F., Backer, J.M., Hyman, A.A., and Zerial, M. (1999). Rab5 regulates motility of early endosomes on microtubules. Nat. Cell Biol. *1*, 376–382.

Ortiz, D., Medkova, M., Walch-Solimena, C., and Novick, P. (2002). Ypt32 recruits the Sec4p guanine nucleotide exchange factor, Sec2p, to secretory vesicles; evidence for a Rab cascade in yeast. J. Cell Biol. *157*, 1005–1015. Published online June 3, 2002. 10.1083/jcb.200201003.

Palade, G. (1975). Intracellular aspects of the process of protein synthesis. Science *189*, 347–358.

Pelkmans, L., and Helenius, A. (2003). Insider information: what viruses tell us about endocytosis. Curr. Opin. Cell Biol. *15*, 414–422.

Peterson, M.R., and Emr, S.D. (2001). The class c vps complex functions at multiple stages of the vacuolar transport pathway. Traffic *2*, 476–486.

Pfeffer, S.R. (2001). Rab GTPases: specifying and deciphering organelle identity and function. Trends Cell Biol. *11*, 487–491.

Poupon, V., Stewart, A., Gray, S.R., Piper, R.C., and Luzio, J.P. (2003). The role of mVps18p in clustering, fusion, and intracellular localization of late endocytic organelles. Mol. Biol. Cell *14*, 4015–4027. Published online July 11, 2003. 10.1091/mbc.E03-01-0040.

Price, A., Seals, D., Wickner, W., and Ungermann, C. (2000). The docking stage of yeast vacuole fusion requires the transfer of pro-

teins from a cis-SNARE complex to a Rab/Ypt protein. J. Cell Biol. *148*, 1231–1238.

Richardson, S.C., Winistorfer, S.C., Poupon, V., Luzio, J.P., and Piper, R.C. (2004). Mammalian late vacuole protein sorting orthologues participate in early endosomal fusion and interact with the cytoskeleton. Mol. Biol. Cell *15*, 1197–1210. Published online December 10, 2003. 10.1091/mbc.E03-06-0358.

Rieder, S.E., and Emr, S.D. (1997). A novel RING finger protein complex essential for a late step in protein transport to the yeast vacuole. Mol. Biol. Cell *8*, 2307–2327.

Rothman, J.E., and Sollner, T.H. (1997). Throttles and dampers: controlling the engine of membrane fusion. Science *276*, 1212–1213.

Salzman, N.H., and Maxfield, F.R. (1989). Fusion accessibility of endocytic compartments along the recycling and lysosomal endocytic pathways in intact cells. J. Cell Biol. *109*, 2097–2104.

Schekman, R., and Orci, L. (1996). Coat proteins and vesicle budding. Science *271*, 1526–1533.

Schmid, S.L., Fuchs, R., Male, P., and Mellman, I. (1988). Two distinct subpopulations of endosomes involved in membrane recycling and transport to lysosomes. Cell *52*, 73–83.

Seals, D.F., Eitzen, G., Margolis, N., Wickner, W.T., and Price, A. (2000). A Ypt/Rab effector complex containing the Sec1 homolog Vps33p is required for homotypic vacuole fusion. Proc. Natl. Acad. Sci. USA *97*, 9402–9407.

Sollner, T., Whiteheart, S.W., Brunner, M., Erdjument-Bromage, H., Geromanos, S., Tempst, P., and Rothman, J.E. (1993). SNAP receptors implicated in vesicle targeting and fusion. Nature *362*, 318–324.

Sonnichsen, B., De Renzis, S., Nielsen, E., Rietdorf, J., and Zerial, M. (2000). Distinct membrane domains on endosomes in the recycling pathway visualized by multicolor imaging of Rab4, Rab5, and Rab11. J. Cell Biol. *149*, 901–914.

Stenmark, H., Parton, R.G., Steele-Mortimer, O., Lutcke, A., Gruenberg, J., and Zerial, M. (1994). Inhibition of rab5 GTPase activity stimulates membrane fusion in endocytosis. EMBO J. *13*, 1287–1296.

Stoorvogel, W., Strous, G.J., Geuze, H.J., Oorschot, V., and Schwartz, A.L. (1991). Late endosomes derive from early endosomes by maturation. Cell *65*, 417–427.

van der Sluijs, P., Hull, M., Webster, P., Male, P., Goud, B., and Mellman, I. (1992). The small GTP-binding protein rab4 controls an early sorting event on the endocytic pathway. Cell *70*, 729–740.

Verestoy, J., Chetverikov, D., and Marcell, N. (1999). Digital particle image velocimetry: a challenge for feature based tracking. Machine Graphics and Vision *8*, 553–569.

Vieira, O.V., Botelho, R.J., and Grinstein, S. (2002). Phagosome maturation: aging gracefully. Biochem. J. *366*, 689–704.

Ward, E.S., Martinez, C., Vaccaro, C., Zhou, J., Tang, Q., and Ober, R.J. (2005). From sorting endosomes to exocytosis: association of Rab4 and Rab11 GTPases with the Fc receptor, FcRn, during recycling. Mol. Biol. Cell *16*, 2028–2038. Published online February 2, 2005. 10.1091/mbc.E04-08-0735.

Wurmser, A.E., Sato, T.K., and Emr, S.D. (2000). New component of the vacuolar class C–Vps complex couples nucleotide exchange on the Ypt7 GTPase to SNARE-dependent docking and fusion. J. Cell Biol. *151*, 551–562.

Zerial, M., and McBride, H. (2001). Rab proteins as membrane organizers. Nat. Rev. Mol. Cell Biol. *2*, 107–117.